Engineering Solid Mechanics12 (2024) 141-156

Contents lists available atGrowingScience

Engineering Solid Mechanics

homepage: www.GrowingScience.com/esm

A new framework for optimizing energy harvesting from smart composites integrated with piezoelectric patches utilizing lamination parameters

Mustafa Kemal Acar[a] and Peyman Lahe Motlagh[a*]

[a]*Department of Mechanical Engineering, Gebze Technical University, Kocaeli, Turkey*

ARTICLEINFO

Article history:
Received 2 July 2023
Accepted 18 October2 023
Available online
18 October 2023

Keywords:
Composite panel
Energy Harvesting
Optimization
Piezoelectric patches

ABSTRACT

Amongst various structures, 2D panels are widely used in many industries and in each application, there are many ambient vibrations which can be converted into electrical energy. The very efficient method to utilize can be using piezoelectric patches which are stuffiest enough for various applications like energy harvesting. This study presents a novel approach for investigating energy harvesting in smart structures using composite panels integrated with piezoelectric patches. The panels are chosen to symmetry-balanced laminated composites, and modal and harmonic analysis conducted using the Rayleigh-Ritz method. To compute the kinetic and potential energy components of the piezoelectric patches at a local level, piecewise Heaviside functions are employed, and these energy components are integrated into the equations of motion together with those of the host composite plate. The results of the numerical method are validated by a commercial finite element software (FEM) COMSOL and there is a good match between FEM and this paper results. By subjecting the laminated composite with piezoelectric patches to forced vibration while varying the lamination parameter, the power output is optimized. The findings emphasize the substantial impact of the lamination parameter on power output, indicating that modifications can result in significant power output increase.

1. Introduction

In recent years, there has been a growing demand for efficient and sustainable energy harvesting technologies to meet the ever-increasing energy needs of modern society. Among various approaches, the integration of piezoelectric materials into composite structures has shown great potential for converting ambient mechanical vibrations into usable electrical energy (Detwiler et al., 1995). This integration enables the development of smart materials capable of self-powered sensing systems, wireless sensor networks, and other energy-autonomous devices (Wan et al., 2023). The purpose of using laminated composites is to combine the desirable properties of different materials and create a composite material with improved overall performance. Each layer in the laminate may contribute specific characteristics, such as high strength, stiffness, impact resistance, or thermal stability, depending on the materials used (Park et al., 2001). By strategically arranging and bonding these layers, engineers can tailor the properties of the laminated composite to meet specific requirements for a given application(Park et al., 2001). One key advantage of laminated composites is their ability to provide high strength and stiffness while maintaining a low weight. This is particularly important in industries such as aerospace, automotive, and sports equipment manufacturing, where lightweight materials are essential for achieving fuel efficiency, performance, and durability(Liu, 2023).

Various methods and technologies are utilized for harvesting energy from vibrations, depending on the application and needs. These methods include piezoelectric (Kim et al., 2011), electromagnetic (Yang et al., 2009), and electrostatic transduction mechanisms (Torres & Rincon-Mora, 2009), which are commonly employed in vibration energy harvesting.

* Corresponding author.
E-mail addresses: peyman.lahe@gtu.edu.tr (P. L. Motlagh)

ISSN 2291-8752 (Online) - ISSN 2291-8744 (Print)

doi: 10.5267/j.esm.2023.10.003

Their small form factor allows for easy integration into various systems without adding significant bulk or weight. These materials are known for their durability and robustness, making them suitable for long-term and reliable operation in harsh environmental conditions. These materials have gained significant attention and adoption across various applications, including structural health monitoring (Jiao et al., 2020), energy harvesting (Safaei et al., 2019), and shunt damping (Han et al., 2013). Piezoelectric materials exhibit a wide frequency response range, allowing them to harvest energy from a broader spectrum of vibrations (Fakhzan & Muthalif, 2013). This flexibility in frequency response makes them suitable for capturing energy from various vibration sources, including low-frequency ambient vibrations and high-frequency mechanical vibrations. Piezoelectric energy harvesters can be relatively easier to manufacture compared to electromagnetic or electrostatic counterparts(Cook-Chennault et al., 2008). Piezoelectric materials, such as ceramics or polymers, can be readily integrated into devices or structures, making the manufacturing process more straightforward and cost-effective. Piezoelectric energy harvesters can be designed to be compact and lightweight, which is advantageous for applications where size and weight constraints are critical, such as wearable devices or portable electronics (Lam et al., 1997). They can withstand mechanical stresses, temperature variations, and other challenging operating conditions, ensuring the longevity and performance stability of the energy harvesting system(Li et al., 2014).

Energy harvesting has been a primary focus of research by (Motlagh et al., 2021) highlighting the potential of piezoelectric materials in this design domain. The generated voltage difference can be effectively captured and subsequently utilized as a viable source of electrical energy(Howells, 2009). The performance of piezoelectric energy harvesting systems is contingent upon several crucial factors that significantly influence their overall efficiency and effectiveness. The geometric attributes of the piezoelectric material can be meticulously engineered to optimize its electrical properties and enhance the energy conversion process (H. Yang et al., 2017). Moreover, the frequency and amplitude of the mechanical vibrations directly influence the magnitude and quality of the electrical energy output. A comprehensive understanding of the intricate interplay between these vibrational parameters and the resulting energy harvesting performance is crucial for devising effective optimization strategies (Motlagh et al., 2020). Piezoelectric materials, in the form of patches or layers, are predominantly employed in the field of structural engineering for their integration onto the surfaces of flexible beam or plate-like structures (Lahe Motlagh et al., 2023; Motlagh et al., 2021). In this research study focuses on the investigation of energy harvesting techniques through the integration of vibrating laminated composite plates with piezoelectric patches. In existing literature, researchers have made significant contributions to the modeling of structures integrated with piezoelectric materials. Initially, Erturk and Inman (2009) proposed a lumped parameter model for beam-like structures with a full piezoelectric layer. Expanding upon this work, Motlagh et al. (2018) and Yoon et al. (2016) developed an analytical model for plate-like structures incorporating a piezoelectric patch, which can also be adapted for partially covered panels. Additionally, (Zhou et al., 2018) focused on smart composite modeling and presented a novel approach for analyzing the vibration behavior of a composite pipe-shaped structure integrated with piezoelectric materials.

Power optimization plays a vital role in improving the efficiency and viability of energy harvesting systems, as it directly affects the amount of electrical energy that can be generated and utilized. One promising avenue for enhancing power output is through the manipulation of lamination parameters within the composite structure. Lamination parameters include factors such as the stacking sequence, fiber orientations, and layer thicknesses, which collectively determine the mechanical and electromechanical properties of the laminated composite (Almeida & Awruch, 2009). By strategically selecting and optimizing these parameters, it is possible to tailor the structural response and enhance the electromechanical coupling efficiency, thereby maximizing power output. Various researchers have employed the lamination parameters technique to represent the stiffness characteristics of laminated composites in a concise form, irrespective of the number of layers and their individual thicknesses. Abdalla et al. (2007) utilized lamination parameters to express the fundamental natural frequency of symmetrically laminated panels. Trias et al. (2016) employed lamination parameters to determine the optimal stacking sequence that maximizes the fundamental frequency. Honda et al. (2009) optimized lamination parameters to modify the natural frequencies of laminates based on three performance metrics. (Bardell et al., 1997) conducted a vibration analysis of thin, laminated, cylindrically singly curved shell panels using the finite element method. Assaee and Hasani (2015) investigated the forced vibration response of curved composite cylindrical shells using the spline finite strip method.

The optimization of power output in laminated composites integrated with piezoelectric patches via lamination parameters is a complex and multifaceted research area. It requires a comprehensive understanding of the interplay between the mechanical and electrical properties, as well as the effects of different lamination configurations on the overall system performance. Consequently, this topic has attracted considerable attention from researchers in the field of smart materials and energy harvesting. In the existing body of literature, several approaches have been proposed for modeling piezoelectric laminated composite plates. One widely employed method is Classical Plate Theory (CPT), which is a two-dimensional mathematical model designed to analyze thin plates with small deformations. CPT assumes a thin and uniformly thick plate, neglecting deformations in the thickness direction compared to those in the plate's plane(Lee, 1990). While CPT possesses certain limitations, such as its inability to accurately model large deformations and shear effects, it remains a prevalent choice for modeling straight panels. Researchers have developed various CPT-based models to investigate the vibration characteristics of piezoelectric layers (Zhang & Yang, 2009). To optimize the lamination parameter for a specific application, a combination of numerical modeling techniques can be employed. Finite Element Analysis (FEA) is a numerical method capable of simulating the panel's behavior and offering insights into the influence of various lamination parameters on energy

harvesting performance. FEA facilitates the calculation of displacement, strain, and electric potential, providing a comprehensive understanding of the panel's electromechanical behavior. Moreover, FEA enables the evaluation of panel performance under different loading conditions, including static and dynamic loads (David Müzel et al., 2020).

Enhancing the efficiency and reliability of piezoelectric energy harvesting systems remains an ongoing challenge. The energy generated from smart composites has received limited attention thus far. To address this, the present study proposes an approach to optimize the power output of a smart panel integrated with piezoelectric patches by selecting an appropriate lamination parameter for the panel. The lamination parameter, dictating the stacking sequence of the panel's different layers, significantly impacts the piezoelectric effect and energy harvesting performance. In this study, the Rayleigh-Ritz Method is employed to calculate the natural frequencies and mode shapes of a smart composite panel with piezoelectric patches. The analytical model incorporates the geometric discontinuities of the piezoelectric patches and utilizes piecewise Heaviside functions to obtain the kinetic and potential energy components locally. These components are combined with those of the host composite plate to derive the equations of motion. Furthermore, the governing equation of motion is derived using Hamilton's principle. To ensure the accuracy and reliability of the analytical model, the obtained results are validated by comparing them with a commercial FEM software, COMSOL. Additionally, optimizations are performed to obtain globally optimal results. The optimized lamination parameter is then compared with the original unidirectional configuration to illustrate the benefits of lamination optimization. Through this comprehensive research, it aims to contribute to the advancement of power optimization techniques in laminated composites integrated with piezoelectric patches. The findings will provide insights into the influence of lamination parameters on energy harvesting performance, facilitating the design and development of efficient and practical energy harvesting systems. These advances will contribute to the broader goal of realizing self-powered devices and enabling sustainable energy solutions in various engineering applications.

2. Method

To solve equation of motion in the smart structure we have in this paper, classical plate theory is utilized to implement motion of smart composite integrated with piezoelectric patches. Subsequently, the constitutive equations for the problem's structural utilize lamination parameters to include effect of composite stacking sequence. To present symmetry-balanced this study use Miki's lamination diagram to include various lamination parameters such that the whole design space is simplified.

3. Problem Definition

Piezoelectric materials are commonly employed as patches or layers integrated onto the surfaces of flexible structures that resemble beams or plates. The diagram presented in Fig. 1. illustrates a schematic representation of a fully clamped composite plate, where a pair of piezo patches is attached to it in a bimorph configuration. The plate's dimensions are characterized by the parameters a, b, and h_s, where a and b correspond to the length and width of the plate, respectively, and h_s represents the overall thickness of the plate. The composite plate comprises layers of equal thickness. The length, width, and thickness of the piezo patches are denoted by l_p, w_p, and h_p, respectively. Symmetrically positioned with respect to the plate's mid-plane, both piezo patches are symmetrically attached to the top and bottom surfaces of the laminated composite plate. These piezo patches are connected in parallel to a resistive load, represented by R_l. Occupying a rectangular region on the composite plate, the piezo patches are defined by the coordinates of their two corners, (x_1, y_1) and (x_2, y_2). To perform frequency response analyses, a transverse harmonic point force is applied at the coordinates (x_0, y_0), acting as the excitation source.

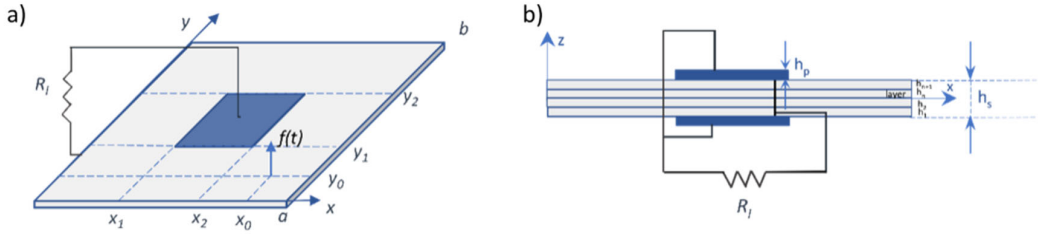

Fig. 1. Schematic representation of a laminated composite plate with surface-bonded piezo patches: Isometric view, (b) Cross-sectional view

4. Constitutive Equations

Piezoelectric patches are commonly fabricated as thin plates, which enables the use of a two-dimensional Kirchhoff plate model to represent the mechanical behavior of the patch's skin. According to Kirchhoff plate theory, this model assumes that the deflection of the middle surface is significantly smaller than the thickness of the plate. Initially, the cross-sectional plane of the piezoelectric patch is perpendicular to the middle surface, and this orientation remains unchanged even after the plate undergoes bending. As a result of this assumption, the transverse shear strains γ_{zx} and γ_{yz}, which represent the deformation in the directions perpendicular to the plate's surface, can be neglected. Similarly, the normal strain ε_{zz}, which corresponds to the deformation occurring in the thickness direction of the plate, can also be disregarded when analyzing transverse vibrations

of the skin thus the normal stress σ_{zz} in the thickness direction being significantly smaller than the stresses occurring within the plane of the plate. Accordingly, the plane stress state:

$$\sigma_{zz} = \tau_{yz} = \tau_{zx} = 0 \tag{1}$$

The structural layer material is assumed to exhibit isotropic behavior. In the context of Kirchhoff plate theory, the relationship between stress and strain for a thin composite plate is expressed as follows.

$$\begin{pmatrix} \sigma_{xx} \\ \sigma_{yy} \\ \tau_{xy} \end{pmatrix} = \frac{Y_s}{1-\upsilon_s{}^2} \begin{bmatrix} 1 & \upsilon_s & 0 \\ \upsilon_s & 1 & 0 \\ 0 & 0 & \frac{1-\upsilon_s}{2} \end{bmatrix} \begin{pmatrix} \varepsilon_{xx} \\ \varepsilon_{yy} \\ \gamma_{xy} \end{pmatrix} \tag{2}$$

In this context, Y_s represents the Young's modulus and ν_s corresponds to the Poisson's ratio of the structural layer. By employing the principle of equilibrium, we equate the force and moment to the integral of the stress and stress multiplied by the distance from the centerline. Fig. 2. And Fig. 3. show the forces and moments for the classical lamination theory.

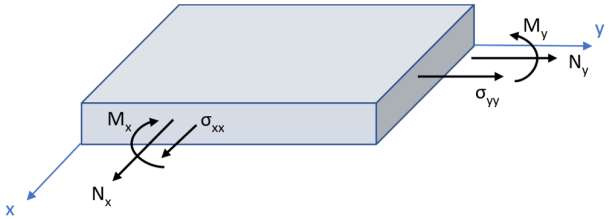

Fig. 2. In plane normal forces and bending moment

$$N_x = \int_{-h/2}^{h/2} \sigma_x \, dz \tag{3}$$

In this equation, h represents the thickness of the plate and z shows thickness directions. If expressed in compact form:

$$\begin{Bmatrix} N_x \\ N_y \\ N_{xy} \end{Bmatrix} = \int_{-h/2}^{h/2} \begin{Bmatrix} \sigma_x \\ \sigma_y \\ \tau_{xy} \end{Bmatrix} dz \tag{4}$$

and moment resultants can be expressed as follows:

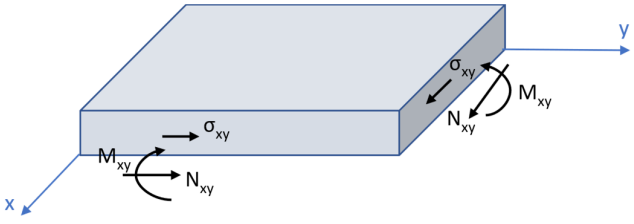

Fig. 3. In- plane shear force and twisting moment

$$\begin{Bmatrix} M_x \\ M_y \\ M_{xy} \end{Bmatrix} = \int_{-h/2}^{h/2} \begin{Bmatrix} \sigma_x \\ \sigma_y \\ \tau_{xy} \end{Bmatrix} z \, dz \tag{5}$$

Herein, the integration is performed across the entire thickness of the laminate by summing the integrals over each individual layer. So, the integrals are taken as follows and Fig. 4. shows notation for location of ply interfaces.

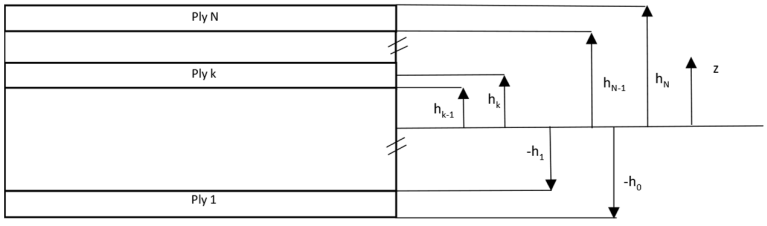

Fig. 4. Notation for location of ply interfaces

$$\begin{Bmatrix} N_x \\ N_y \\ N_{xy} \end{Bmatrix} = \sum_{k=1}^{N} \int_{h_{k-1}}^{h_k} \begin{Bmatrix} \sigma_x \\ \sigma_y \\ \tau_{xy} \end{Bmatrix} dz \tag{6}$$

$$\begin{Bmatrix} M_x \\ M_y \\ M_{xy} \end{Bmatrix} = \sum_{k=1}^{N} \int_{h_{k-1}}^{h_k} \begin{Bmatrix} \sigma_x \\ \sigma_y \\ \tau_{xy} \end{Bmatrix} z dz \tag{7}$$

By utilizing these integrals, the equations can be formulated in a conventional manner, establishing a relationship between stress resultants, moment resultants, centerline strains, and curvatures in the following expression:

$$\begin{Bmatrix} N \\ M \end{Bmatrix} = \begin{bmatrix} A & B \\ B & D \end{bmatrix} \begin{Bmatrix} \varepsilon^0 \\ K \end{Bmatrix} \tag{8}$$

The vector ε_0 represents the mid-plane strains, while K represents the panel curvatures. $A, B,$ and D are tensors that respectively represent the in-plane stiffness, in-plane/bending coupling, and bending stiffness. The relationship between force and moment resultants and the strains in the laminate can be established by considering the material properties of each ply group. In the case of symmetric laminates, the in-plane/bending coupling tensor is zero, the B matrix is equal to zero. It is possible to represent the normalized in-plane stiffness tensor using only two lamination parameter variables, that can be formulated (Tsai & Hahn, n.d.). The normalized lamination parameters, denoted as V_1 and V_3, can be defined as follows:

$$V_1 = \frac{1}{h} \sum_{k=1}^{N_l} t_k \cos(2\theta_k) \tag{9}$$

$$V_3 = \frac{1}{h} \sum_{k=1}^{N_l} t_k \cos(4\theta_k) \tag{10}$$

N_l is the number of layers, t_k's are the layer thicknesses, and θ_k's are the layer angles. The material invariants, denoted as U's, are calculated using the following equation:

$$\begin{Bmatrix} U_1 \\ U_2 \\ U_3 \\ U_4 \\ U_5 \end{Bmatrix} = \begin{bmatrix} \frac{3}{8} & \frac{3}{8} & \frac{1}{4} & \frac{1}{2} \\ \frac{1}{2} & -\frac{1}{2} & 0 & 0 \\ \frac{1}{8} & \frac{1}{8} & -\frac{1}{4} & -\frac{1}{2} \\ \frac{1}{8} & \frac{1}{8} & \frac{3}{4} & -\frac{1}{2} \\ \frac{1}{8} & \frac{1}{8} & -\frac{1}{4} & \frac{1}{2} \end{bmatrix} \begin{Bmatrix} Q_{11} \\ Q_{22} \\ Q_{12} \\ Q_{66} \end{Bmatrix} \tag{11}$$

The reduced stiffness matrix entities, Q_{ij}'s, are given by the following equation:

$$\begin{Bmatrix} Q_{11} \\ Q_{22} \\ Q_{12} \\ Q_{66} \end{Bmatrix} = \begin{Bmatrix} \frac{E_1}{\gamma} \\ \frac{E_2}{\gamma} \\ \frac{v_{12}E_2}{\gamma} \\ \frac{G_{12}}{\gamma} \end{Bmatrix} \text{ where } \gamma = (1 - v_{12}v_{21}) \tag{12}$$

By employing the reciprocity relations for orthotropic layers, the Minor Poisson's ratio can be determined as follows:

$$v_{21} = \frac{v_{12}E_2}{E_1} \tag{13}$$

Using the normalized lamination parameters V_1 and V_3 found by Eq. (9) and Eq. (10), it is possible to represent the normalized in-plane stiffness tensor.

$$\frac{A}{h} = \begin{bmatrix} U_1 & U_4 & 0 \\ U_4 & U_1 & 0 \\ 0 & 0 & U_5 \end{bmatrix} + \begin{bmatrix} U_2 & 0 & 0 \\ 0 & -U_2 & 0 \\ 0 & 0 & 0 \end{bmatrix} V_1 + \begin{bmatrix} U_3 & -U_3 & 0 \\ -U_3 & U_3 & 0 \\ 0 & 0 & -U_3 \end{bmatrix} V_3 \tag{14}$$

For laminates composed of numerous uniformly distributed layers, the bending stiffness matrix becomes orthotropic, characterized by only two lamination parameter variables. This leads to the following relation (Fukunaga, & Vanderplaats):

$$D = \frac{A\,h^2}{12} \tag{15}$$

The electric field E_{33} is utilized in the subsequent steps in the following manners:

$$E_{33} = -\frac{v_i(t)}{h_p} \tag{16}$$

By virtue of the electric field and its alignment with the z-axis, the electric displacement field D can be simplified to a scalar component, denoted as D_3. In relation to each piezo-patch, the stress and electric displacement components can be adequately characterized using 2D constitutive equations, as detailed in the study conducted by (Yoon et al., 2016).

$$\begin{pmatrix} \sigma_{xx} \\ \sigma_{yy} \\ \tau_{xy} \\ D_3 \end{pmatrix} = \begin{bmatrix} \bar{c}_{11} & \bar{c}_{12} & 0 & -\bar{e}_{31} \\ \bar{c}_{12} & \bar{c}_{11} & 0 & -\bar{e}_{31} \\ 0 & 0 & \bar{c}_{66} & 0 \\ \bar{e}_{31} & \bar{e}_{31} & 0 & \bar{\varepsilon}^{s}_{33} \end{bmatrix} \begin{pmatrix} \varepsilon_{xx} \\ \varepsilon_{yy} \\ \gamma_{xy} \\ E_{33} \end{pmatrix} \tag{17}$$

Within this equation, the term $\bar{c}_{ij}$ denotes the reduced modulus of elasticity associated with the piezoelectric patches. The equations of motion governing the system are derived by employing Hamilton's principle, as:

$$\delta \oint_{t_1}^{t_2} \left(KE - PE + W_p\right) dt = 0 \tag{18}$$

where δ signifies a variation in the system's configuration, KE represents the system's kinetic energy, PE represents the system's potential energy, W_p denotes the work done by non-conservative forces, and the integral is taken over a specified time interval from t_1 t, t_2. The derivation of the expression for the kinetic energy of the system can be obtained in the following manner:

$$KE = \frac{1}{2} \iint_S m(x.y)\dot{w}^2\, dS \tag{19}$$

The parameter S denotes the surface area of the system, which includes both the upper surfaces of the piezo-patches and the thin composite plate. The variables $m(x,y)$ and $\dot{w}$ represent the areal mass and velocity terms, respectively. The calculation for determining the equivalent mass per unit area can be accomplished by employing the following computation:

$$m(x.y) = \rho_s h_s + \rho_p h_p P(x.y) \tag{20}$$

In this context, ρ_s and ρ_p represent the respective densities of the thin composite plate and piezoelectric patch. The function $P\ (x,y)$ serves as an indicator, identifying the specific locations on the surface of the composite plate where k piezoelectric patches have been affixed.

$$P(x.y) = \sum_{i=1}^{k} [H(x - x_{i.1}) - H(x - x_{i.2})] \times [H(y - y_{i.1}) - H(y - y_{i.2})] \tag{21}$$

In Fig. 2. the geometrical parameters of the piezoelectric patch are illustrated. The formula for the area, defined by the four vertices x_1, x_2, y_1, and y_2 along the x and y-axes, incorporates the use of the Heaviside unit step function denoted by H.

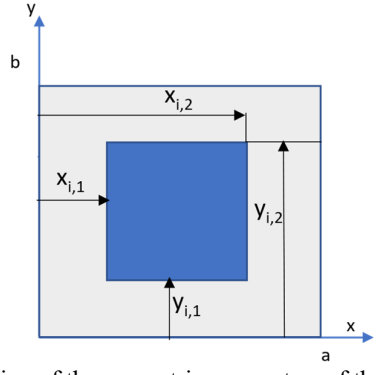

Fig. 2. Representation of the geometric parameters of the piezoelectric patch

The stored potential energy within the composite plate and piezoelectric patch is represented by the symbol PE, and it is expressed in the following manner:

$$PE = \frac{1}{2}\iiint_{V_s}\left\{(\sigma_{xx}\varepsilon_{xx})_s + (\sigma_{yy}\varepsilon_{yy})_s + (\tau_{xy}\gamma_{xy})_s\right\}dV_s + \frac{1}{2}\iiint_{V_p}\left\{(\sigma_{xx}\varepsilon_{xx})_p + (\sigma_{yy}\varepsilon_{yy})_p + (\tau_{xy}\gamma_{xy})_p\right\}dV_p \tag{22}$$

In this equation, the thin composite plate and the piezoelectric patch are characterized by their respective volumes, denoted as V_s and V_p. The potential energy stored within the thin composite plate can be mathematically described in the following way:

$$PE_S = \frac{1}{2}\iint_{S_s}\left\{D_{11}\left(\frac{\partial^2 w}{\partial x^2}\right)^2 + 2D_{12}\left(\frac{\partial^2 w}{\partial y^2}\right)\left(\frac{\partial^2 w}{\partial x^2}\right) + D_{22}\left(\frac{\partial^2 w}{\partial y^2}\right)^2 + 4D_{16}\left(\frac{\partial^2 w}{\partial x^2}\right)\left(\frac{\partial^2 w}{\partial x\partial y}\right) + 4D_{26}\left(\frac{\partial^2 w}{\partial y^2}\right)\left(\frac{\partial^2 w}{\partial x\partial y}\right) + 4D_{66}\left(\frac{\partial^2 w}{\partial x\partial y}\right)^2\right\}dS_s \tag{23}$$

The equation provided involves two key elements: S_s, which denotes the surface area of a thin composite plate, and D_{ij}, which represents the elements of the bending stiffness matrix of a host plate consisting of *n* layers that obtained through the following derivation:

$$D_{ij} = \frac{1}{3}\sum_{k=1}^{n}(Q_{ij})_k\,(z_k^3 - z_{k-1}^3).\ \text{for } i = j = 1.2.6 \tag{24}$$

The elements of the reduced stiffness matrix, denoted as Q_{ij}'s, can be determined by employing Eqs. (12-14). The stored potential energy within the thin piezoelectric patches can be represented by the following expression.

$$PE_P = \frac{1}{2}\sum_{l=1}^{2}\iint_{S_p} P(x.y)\left\{D_{11}^p\left(\frac{\partial^2 w}{\partial x^2}\right)^2 + 2D_{12}^p\left(\frac{\partial^2 w}{\partial y^2}\right)\left(\frac{\partial^2 w}{\partial x^2}\right) + D_{11}^p\left(\frac{\partial^2 w}{\partial y^2}\right)^2 + 4D_{66}^p\left(\frac{\partial^2 w}{\partial xy}\right)^2 - \bar{e}_{31}v(t)\left(\frac{h_s + h_p}{2}\right)\left(\frac{\partial^2 w}{\partial x^2} + \frac{\partial^2 w}{\partial y^2}\right)\right\}dS_p \tag{25}$$

In this equation, S_p denotes the surface area of the piezoelectric patches, *v(t)* represents the voltage applied to the patches, and D_{ij}^p corresponds to the bending stiffness matrix of the patches, which can be defined as follows.

$$\begin{aligned} D_{11}^p &= \int_{\frac{h_s}{2}}^{\frac{h_s}{2}+h_p}\bar{c}_{11}\,z^2dz = \int_{-\frac{h_s}{2}-h_p}^{-\frac{h_s}{2}}\bar{c}_{11}\,z^2dz = \bar{c}_{11}\left(\frac{h_p^3}{3} + \frac{h_s^2h_p}{4} + \frac{h_sh_p^2}{2}\right) \\ D_{12}^p &= \int_{\frac{h_s}{2}}^{\frac{h_s}{2}+h_p}\bar{c}_{12}\,z^2dz = \int_{-\frac{h_s}{2}-h_p}^{-\frac{h_s}{2}}\bar{c}_{12}\,z^2dz = \bar{c}_{12}\left(\frac{h_p^3}{3} + \frac{h_s^2h_p}{4} + \frac{h_sh_p^2}{2}\right) \\ D_{66}^p &= \int_{\frac{h_s}{2}}^{\frac{h_s}{2}+h_p}\bar{c}_{66}\,z^2dz = \int_{-\frac{h_s}{2}-h_p}^{-\frac{h_s}{2}}\bar{c}_{66}\,z^2dz = \bar{c}_{66}\left(\frac{h_p^3}{3} + \frac{h_s^2h_p}{4} + \frac{h_sh_p^2}{2}\right) \end{aligned} \tag{26}$$

The work done by the point force can be calculated by the following equation.

$$W_p = \iint_S f(t)\delta(x - x0)\delta(y - y0)\,dS \tag{27}$$

In this equation, $f(t)$ denotes the amplitude of the force, and $\delta(x)$ and $\delta(y)$ represent the Dirac delta functions along the *x* and *y* axes, respectively. The displacement of the system is denoted by w. By considering these variables, we can derive the equation of motion for the plate and piezoelectric patches as follows:

$$m(x.y)\ddot{w}+\begin{bmatrix}\left\{D_{11}+P(x.y)2D_{11}^{p}\right\}\left(\frac{\partial^2 w}{\partial x^2}\right)^2+\left\{\left(4D_{12}^{p}P(x.y)+2D_{12}\right)\left(\frac{\partial^2 w}{\partial y^2}\right)\left(\frac{\partial^2 w}{\partial x^2}\right)\right\}\\ +\left(P(x.y)2D_{11}{}^{p}+D_{22}\right)\left(\frac{\partial^2 w}{\partial y^2}\right)^2+(4D_{16})\frac{\partial^2 w}{\partial x^2}\left(\frac{\partial^2 w}{\partial x\partial y}\right)\\ +(4D_{26})\left(\frac{\partial^2 w}{\partial y^2}\right)\left(\frac{\partial^2 w}{\partial x\partial y}\right)+\left(4D_{66}+8D_{66}^{p}P(x.y)\right)\left(\frac{\partial^2 w}{\partial x\partial y}\right)^2\end{bmatrix}-\frac{2\ \bar{e}_{31}v(t)\left(h_s+h_p\right)}{2}P(x.y)\left(\frac{\partial^2 w(x.y)}{\partial x^2}+\frac{\partial^2 w(x.y)}{\partial y^2}\right)=f(t)\delta(x-x0)\delta(y-y0) \tag{28}$$

5. Miki's lamination diagram

Miki's Lamination Diagram is a graphical tool used in the field of composite materials to analyze and visualize the feasible design space for balanced and symmetric laminates (Albazzan et al., 2019). The diagram consists of two axes that represent the normalized lamination parameters, typically denoted as V_1 and V_3. These parameters are calculated based on the angle and thickness of each layer within the laminate. By plotting various combinations engineers can determine the allowable range of lamination configurations that satisfy specific design requirements. Points within this region represent viable laminate designs that fulfill balance and symmetry conditions. The boundary of the diagram is defined by the curve given below, which separates the feasible area from the non-feasible area.

$$V_3 = 2V_1^2 - 1 \tag{29}$$

In Fig. 6. Miki's Lamination Diagram is presented, offering an insightful visual representation. This diagram displays specific points that represent laminates with orientations of [0°], $[\pm 45°]_s$,[90°], and $[0° \pm 45° 90°]_s$ (quasi–isotropic).

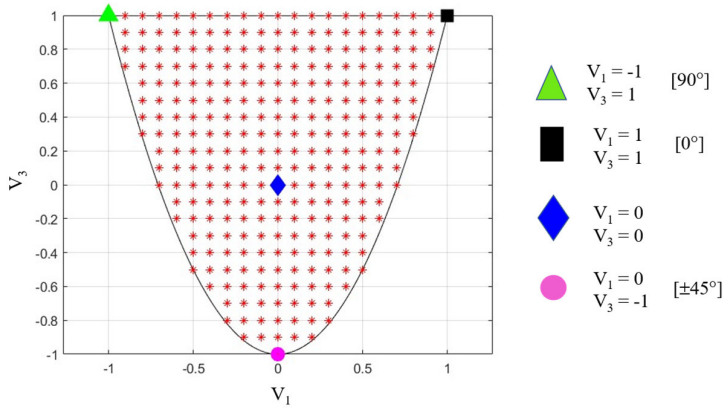

Fig. 6. Miki's Lamination Diagram

7. Modal analysis

Accurately analyzing the piezoelectric energy harvesting (PEH) patches poses challenges due to the presence of geometric inconsistencies at the edges of the piezoelectric patch. To address this issue, the Rayleigh-Ritz method has been employed to conduct modal vibration analysis of a laminated composite plate with integrated piezo-patches. By imposing fully clamped boundary conditions (CCCC), the natural frequencies and their corresponding mode shapes can be determined for the system. To facilitate the analysis, assumed modes are employed to define the displacement of the system, as described by (Yoon et al., 2016). This approach allows for a comprehensive examination of the system's dynamic characteristics and provides valuable insights into its vibration behavior.

$$w(x.y.t)=\sum_{i=1}^{R}\sum_{j=1}^{N}U_{ij}\,W_{ij}(x.y)\mu_{ij}(t) \tag{30}$$

In the equation provided $\mu_{ij}(t)$, represents the generalized modal coordinates, which are associated with N vibration modes in the y coordinates and R vibration modes in the x coordinates. Assumed modes, $U_{ij}W_{ij}(x,y)$, where U_{ij} represents the corresponding coefficients and $W_{ij}(x,y)$ represents the trial functions that satisfy the boundary conditions. To obtain orthogonal polynomials within the interval $0 \le x < a$, $0 \le y < b$, the Gram-Schmidt procedure is employed such as:

$$\phi_2(x) = (x - B_2)\phi_1(x). \qquad \phi_r(x) = (x - B_r)\phi_{r-1}(x) - C_r\phi_{r-2}(x)$$
$$B_r = \frac{\int_0^a xk(x)\phi_{r-1}^2(x)dx}{\int_0^a k(x)\phi_{r-1}^2(x)dx}. \qquad C_r = \frac{\int_0^a xk(x)\phi_{r-1}(x)\phi_{r-2}(x)dx}{\int_0^a k(x)\phi_{r-2}^2(x)dx} \tag{31}$$

The boundary condition of a rectangular beam with fixed-fixed ends, characterized by the first term of the orthogonal polynomials, denoted as $\phi_1(x)$, can be mathematically obtained through specific techniques which for a fixed-fixed boundary condition for the beam with length a, it can be written as:

$$\phi_1(x) = a^2x^2 - 2ax^3 + x^4. \ \ (0 \le x \le a) \tag{32}$$
$$\varphi_1(x) = b^2y^2 - 2by^3 + y^4. \ \ (0 \le y \le b) \tag{33}$$

The quotient U_{ij} , known as Rayleigh's quotient, can be defined as the ratio between the maximum potential energy and the corresponding reference kinetic:

$$R\left[U_{ij}W_{ij}(x.y)\right] = \frac{PE_{max}}{KE_{ref}} \tag{34}$$

To identify the conditions for achieving a stationary value of Rayleigh's quotient, it is necessary to differentiate it with respect to the coefficients U_{rn}. This process will yield the essential conditions that need to be satisfied for the attainment of stationary value.

$$\frac{\partial R}{\partial U_{ij}} = \left(\frac{\partial PE_{max}}{\partial U_{ij}} - \omega_{ij}^2\frac{\partial KE_{ref}}{\partial U_{ij}}\right) = 0 \tag{35}$$

The maximum potential energy (PE_{max}) and the reference kinetic energy (KE_{ref}) can be determined by utilizing the following equations:

$$PE_{max} = \frac{1}{2}\sum_{i=1}^{N}\sum_{j=1}^{N}\sum_{k=1}^{N}\sum_{l=1}^{N}K_{ij.kl}U_{ij}U_{kl} \tag{36}$$

$$KE_{ref} = \frac{1}{2}\sum_{i=1}^{N}\sum_{j=1}^{N}\sum_{k=1}^{N}\sum_{l=1}^{N}M_{ij.kl}U_{ij}U_{kl} \tag{37}$$

Furthermore, $K_{ij,kl}$, can be identified as:

$$\begin{aligned} K_{ij.kl} = \iint_S [\ &\{D_{11} + 2D_{11}^p P(x.y)\}\left[\frac{\partial^2 W_{ij}}{\partial x^2}\frac{\partial^2 W_{kl}}{\partial x^2}\right] \\ &+\{D_{12} + 2D_{12}^p P(x.y)\}\left[\frac{\partial^2 W_{ij}}{\partial x^2}\frac{\partial^2 W_{kl}}{\partial y^2} + \frac{\partial^2 W_{ij}}{\partial y^2}\frac{\partial^2 W_{kl}}{\partial x^2}\right] \\ &+\{2D_{16}\}\left[\frac{\partial^2 W_{ij}}{\partial x^2}\frac{\partial^2 W_{kl}}{\partial xy} + \frac{\partial^2 W_{ij}}{\partial xy}\frac{\partial^2 W_{kl}}{\partial x^2}\right] \\ &+\{D_{22} + 2D_{11}^p P(x.y)\}\left[\frac{\partial^2 W_{ij}}{\partial y^2}\frac{\partial^2 W_{kl}}{\partial y^2}\right] \\ &+\{2D_{26}\}\left[\frac{\partial^2 W_{ij}}{\partial y^2}\frac{\partial^2 W_{kl}}{\partial xy} + \frac{\partial^2 W_{ij}}{\partial xy}\frac{\partial^2 W_{kl}}{\partial y^2}\right] \\ &+\{4D_{66} + 8D_{66}^p P(x.y)\}\left[\frac{\partial^2 W_{ij}}{\partial xy}\frac{\partial^2 W_{kl}}{\partial xy}\right]]dS \end{aligned} \tag{38}$$

To determine the mass term, $M_{ij,kl}$, one can utilize this equation:

$$M_{ij.kl} = \iint_S W_{ij}(x.y)m(x.y)W_{kl}(x.y)dS \tag{39}$$

After computing the mass and stiffness parameters, the eigenvalue problem for investigating the natural vibration of piezoelectric patches can be formulated as:

$$\left[K_{ij.kl} - \omega_{ij}^2 M_{ij.kl}\right]\left[U_{ij}\right] = \{0\} \tag{40}$$

In this formulation, the eigenvectors of the equation, denoted by U_{ij}'s, represent the coefficients of the assumed mode shapes. The corresponding eigenvalues of the equation are the square of the natural frequencies, denoted by ω_{ij}'s.

8. Electrical circuit equations

Fig. 7. illustrates the representation of the two piezo patches connected to a resistive load in the form of an equivalent circuit. It is important to mention that when nonlinear circuits are utilized in conjunction with the piezo-patches, an alternative

approach known as the equivalent impedance method can be employed, as proposed by (Aghakhani et al., 2019; Motlagh et al., 2021). By applying Kirchhoff's current law, the circuit equation can be formulated:

$$\frac{dv(t)}{dt}\sum_{l=1}^{N}(C_P)_l + \frac{v(t)}{R_l} = \sum_{l=1}^{N} i_l^{\mathrm{p}}(t) \;\; (N = 1.2. \ldots number\ of\ patches) \tag{41}$$

In this equation, the term $i_l^{\mathrm{p}}(t)$ represents the current source that depends on the velocity, $\left(C_p\right)_l$ denotes the equivalent capacitance of the lth piezo-patch, and θ_l corresponds to the electromechanical coupling term for the *l*th piezo-patch. The value of θ_l can be determined through the following procedure.

$$i_l^{\mathrm{p}}(t) = -\theta_l \frac{\partial}{\partial t}\iint_{S_p}\left(\frac{d^2w}{dx^2} + \frac{d^2w}{dy^2}\right)dS_p \tag{42}$$

$$\left(C_p\right)_l = (\bar{\varepsilon}_{33}^{S})\frac{(l_p)(w_p)}{h_p} \tag{43}$$

$$\theta_l = \bar{e}_{31}\left(\frac{h_s + h_p}{2}\right) \tag{44}$$

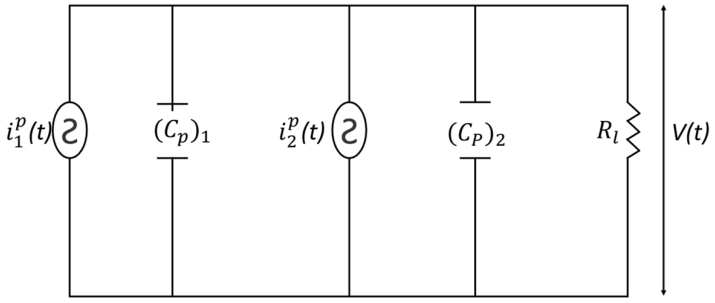

Fig. 7. The representation of the electromechanical system in terms of an equivalent circuit.

9. Harmonic point force excitation and its steady-state responses

By employing a transformation procedure that incorporates modal coordinates, the equations of the system, within physical coordinates, can be effectively converted into modal coordinates. It has been elucidated by (Yoon et al., 2016) that the assumed mode shape coefficients U_{ij} demonstrate orthogonality in relation to the mass and stiffness matrices. This inherent orthogonality property engenders a decoupling effect, thereby yielding uncoupled equations of motion when the system's equations are subjected to the transformation from physical coordinates to modal coordinates.

$$M'_{ij.kl} = U_{ij}^{T} M_{ij.kl} U_{kl} = \begin{cases} 1 & if \;\; ij = kl \\ 0 & if \;\; ij \neq kl \end{cases} \tag{45}$$

$$K'_{ij.kl} = U_{ij}^{T} K_{ij.kl} U_{kl} \;\; = \begin{cases} \omega_{ij}^2 & if \quad ij = kl \\ 0 & if \quad ij \neq kl \end{cases} \tag{46}$$

The modal mass and stiffness matrices, denoted as $M'_{ij,kl}$ and $K'_{ij,kl}$ respectively, play a crucial role in the modal coordinate representation. To determine the applied point force in modal coordinates, a specific procedure needs to be undertaken, involving a series of calculations or computations.

$$f_{rs} = \iint_S f(t)\delta(x - x0)\delta(y - y0)U_{rs}W_{rs}(x.y)dS = f(t)U_{rs}W_{rs}(x0.y0) \tag{47}$$
$$r = 1.2.3. \ldots . N \quad s = 1.2.3. \ldots . N$$

The current output in modal coordinates can be obtained:

$$i_l^{\mathrm{p}}(t) \;\; = -\sum_{r=1}^{N}\sum_{s=1}^{N}\frac{d\mu_{rs}(t)}{dt}\left(\tilde{\theta}_{rs}\right)_l \tag{48}$$

The expression below can be employed to represent the electromechanical coupling term $\left(\tilde{\theta}_{rs}\right)_l$ of the *l*th piezo patch in modal coordinates:

$$\left(\tilde{\theta}_{rs}\right)_l = \theta_l \iint_{S_p} U_{rs}P(x.y)\left(\frac{d^2W_{rs}}{dx^2} + \frac{d^2W_{rs}}{dy^2}\right)dS_p \tag{49}$$

The electromechanically coupled equations of the system can be expressed in modal coordinates in the following manner, as demonstrated by (Gohari et al., 2016):

$$\frac{\partial^2 \mu_{rs}(t)}{\partial t^2} + 2\omega_{rs}\zeta_{rs}\frac{\partial \mu_{rs}(t)}{\partial t} + \omega_{rs}^2 \mu_{rs}(t) - \sum_{l=1}^{2}\left(\tilde{\theta}_{rs}\right)_l v(t) = f_{rs}(t) \tag{50}$$

$$\frac{dv(t)}{dt}\sum_{l=1}^{2}\left(C_p\right)_l + \frac{v(t)}{R_l} + \sum_{l=1}^{2}\sum_{r=1}^{N}\sum_{s=1}^{N}\frac{d\mu_{rs}(t)}{dt}\left(\tilde{\theta}_{rs}\right)_l = 0 \tag{51}$$

In the case of a linear system, when a harmonic force input is applied in the form of $f(t) = F_0 e^{j\omega t}$, the resulting steady-state voltage output and mechanical modal response can be represented as follows:

$$v(t) = Ve^{j\omega t} \tag{52}$$

$$\mu_{rs}(t) = H_{rs}e^{j\omega t} \tag{53}$$

Within this framework, V represents the complex magnitude of the voltage output, and H_{rs} signifies the complex amplitude of the modal response. Upon replacing the values of $\mu_{rs}(t)$, $v(t)$, and f_{rs}, one can derive the complex modal amplitude H_{rs}.

$$H_{rs} = \frac{F_0 U_{rs} W_{rs}(x0.y0) + V\sum_{l=1}^{2}\left(\tilde{\theta}_{rs}\right)_l}{\omega_{rs}^2 - \omega^2 + 2j\zeta_{rs}\omega_{rs}\omega} \tag{54}$$

By employing the same method, the complex voltage amplitude V can be obtained as:

$$V = \frac{-\sum_{l=1}^{2}\sum_{r=1}^{N}\sum_{s=1}^{N}\frac{j\omega\left(\tilde{\theta}_{rs}\right)_l F_0 U_{rs} W_{rs}(x0.y0)}{\omega_{rs}^2 - \omega^2 + 2j\zeta_{rs}\omega_{rs}\omega}}{j\omega\sum_{l=1}^{2}\left(C_p\right)_l + \frac{1}{R_l} + \sum_{l=1}^{2}\sum_{r=1}^{N}\sum_{s=1}^{N}\frac{j\omega\left(\tilde{\theta}_{rs}\right)_l \sum_{l=1}^{2}\left(\tilde{\theta}_{rs}\right)_l}{\omega_{rs}^2 - \omega^2 + 2j\zeta_{rs}\omega_{rs}\omega}} \tag{55}$$

Utilizing a substitution technique like the equation, one can determine the modal displacement of the system in modal coordinates.

$$w(x.y.t) = \sum_{r=1}^{N}\sum_{s=1}^{N}\left(\frac{U_{rs}W_{rs}(x.y)\left[F_0 U_{rs}W_{rs}(x0.y0) + V\sum_{l=1}^{2}\left(\tilde{\theta}_{rs}\right)_l\right]e^{j\omega t}}{\omega_{rs}^2 - \omega^2 + 2j\zeta_{rs}\omega_{rs}\omega}\right) \tag{56}$$

Through the application of a harmonic force input, it becomes possible to derive the frequency response function of the voltage, which illustrates the correlation between the input force and the ensuing voltage output.

$$\frac{v(t)}{F_0 e^{j\omega t}} = \frac{-\sum_{l=1}^{2}\sum_{r=1}^{N}\sum_{s=1}^{N}\frac{j\omega\left(\tilde{\theta}_{rs}\right)_l U_{rs} W_{rs}(x0.y0)}{\omega_{rs}^2 - \omega^2 + 2j\zeta_{rs}\omega_{rs}\omega}}{j\omega\sum_{l=1}^{2}\left(C_p\right)_l + \frac{1}{R_l} + \sum_{l=1}^{2}\sum_{r=1}^{N}\sum_{s=1}^{N}\frac{j\omega\left(\tilde{\theta}_{rs}\right)_l \sum_{l=1}^{2}\left(\tilde{\theta}_{rs}\right)_l}{\omega_{rs}^2 - \omega^2 + 2j\zeta_{rs}\omega_{rs}\omega}} \tag{57}$$

By applying a harmonic force input, one can determine the voltage frequency response function, which expresses the relationship between the input force and the voltage output as:

$$\frac{w(x.y.t)}{F_0 e^{j\omega t}} = \sum_{r=1}^{N}\sum_{s=1}^{N}\left(\frac{U_{rs}W_{rs}(x.y)\left[U_{rs}W_{rs}(x0.y0) + \alpha(\omega)\sum_{l=1}^{2}\left(\tilde{\theta}_{rs}\right)_l\right]}{\omega_{rs}^2 - \omega^2 + 2j\zeta_{rs}\omega_{rs}\omega}\right) \tag{58}$$

10. Technique for separating integrals

In this section, to solve the Rayleigh-Ritz incurred significant computational time, an alternative technique is introduced that involves splitting the integrals (i.e., splitting the surface integral into two separate integrals). Using this method, a significant reduction in computational time can be achieved, especially in scenarios involving higher mode numbers. The variables ε and η represent dimensionless quantities along the x and y coordinates, respectively, as described by the following expressions:

$$\varepsilon = {}^{x}/_{a} \qquad \eta = {}^{y}/_{b} \tag{59}$$

The interpretation the displacement in physical coordinates can be elucidated by considering the normalized variables in characterizing the displacement field (Bhat, 1985) as :

$$w(\varepsilon.\eta.t) = \sum_{m=1}^{N}\sum_{n=1}^{N} U_{mn}X_m(\varepsilon)Y_n(\eta)\mu_{mn}(t) \tag{60}$$

By employing normalized variables, the x and y coordinates can be expressed as orthogonal polynomials $X_m(\varepsilon), Y_n(\eta)$. These polynomials are characterized by coefficient U_{mn} and generalized modal coordinates $\mu_{mn}(t)$. Furthermore, the indicator function $P(\varepsilon,\eta)$ can be split into two separate components.

$$\begin{aligned} &P(\varepsilon.\eta) = P\mathrm{x}(\varepsilon), P\mathrm{y}(\eta) \\ &P\mathrm{x}(\varepsilon) = [H(\varepsilon - x_1/a) - H(\varepsilon - x_2/a)] \\ &P\mathrm{y}(\eta) = \left[H\left(\eta - \frac{y_1}{b}\right) - H\left(\eta - \frac{y_2}{b}\right)\right] \end{aligned} \tag{61}$$

The presence of $P\mathrm{x}(\varepsilon)$ and $P\mathrm{y}(\eta)$ indicates separate Heaviside-step functions operating in the x and y directions. These functions rely on the normalized variables ε and η. An eigenvalue equation can be derived as:

$$\sum_{m=1}^{N}\sum_{n=1}^{N}\left[C_{mnij} - \lambda M_{mnij}\right]U_{mn} = 0\,.\lambda = \rho_s h_s {\omega_{mn}}^2\, a^4/D_{11} \tag{62}$$

The stiffness term C_{mnij} refers to the interaction between the host structure and the piezo patches. It can be defined as:

$$C_{mnij} = Cs_{mnij} + 2Cp_{mnij} \tag{63}$$

The expressions representing the stiffness term of the host structure Cs_{mnij} and the piezo patches Cp_{mnij} can be stated as follows:

$$\begin{aligned} Cs_{mnij} = {} & E_{mi}^{(2.2)}F_{nj}^{(0.0)} + \alpha^4 E_{mi}^{(0.0)}F_{nj}^{(2.2)}\left(\frac{D_{22}}{D_{11}}\right) \\ & + \alpha^2\left[E_{mi}^{(0.2)}F_{nj}^{(2.0)} + E_{mi}^{(2.0)}F_{nj}^{(0.2)}\right]\left(\frac{D_{12}}{D_{11}}\right) \\ & + 2\alpha\left[E_{mi}^{(2.1)}F_{nj}^{(0.1)} + E_{mi}^{(1.2)}F_{nj}^{(1.0)}\right]\left(\frac{D_{16}}{D_{11}}\right) \\ & + 2\alpha^3\left[E_{mi}^{(0.1)}F_{nj}^{(2.1)} + E_{mi}^{(1.0)}F_{nj}^{(1.2)}\right]\left(\frac{D_{26}}{D_{11}}\right) + 4\alpha^2 E_{mi}^{(1.1)}F_{nj}^{(1.1)}\left(\frac{D_{66}}{D_{11}}\right) \end{aligned} \tag{64}$$

$$\begin{aligned} Cp_{mnij} = {} & Ep_{mi}^{(2.2)}Fp_{nj}^{(0.0)}\left(\frac{D_{11}^{p}}{D_{11}}\right) + \alpha^4 Ep_{mi}^{(0.0)}Fp_{nj}^{(2.2)}\left(\frac{D_{22}^{p}}{D_{11}}\right) \\ & + \alpha^2\left[Ep_{mi}^{(0.2)}Fp_{nj}^{(2.0)} + Ep_{mi}^{(2.0)}Fp_{nj}^{(0.2)}\right]\left(\frac{D_{12}^{p}}{D_{11}}\right) \\ & + 4\alpha^2 Ep_{mi}^{(1.1)}Fp_{nj}^{(1.1)}\left(\frac{D_{66}^{p}}{D_{11}}\right) \end{aligned} \tag{65}$$

The aspect ratio ($\alpha = \frac{a}{b}$) characterizes the proportions of the host structure, while the mass term M_{mnij} considers the total mass contributions from the host structure and the piezo patches.

$$M_{mnij} = Ms_{mnij} + 2Mp_{mnij}\ \rho_p h_p/\rho_s h_s \tag{66}$$

In this equation, the mass term of the host structure Ms_{mnij} and the piezo patch Mp_{mnij} can be given by the following expressions:

$$Ms_{mnij} = E_{mi}^{(0.0)}F_{nj}^{(0.0)} \tag{67}$$

$$Mp_{mnij} = Ep_{mi}^{(0.0)}Fp_{nj}^{(0.0)} \tag{68}$$

The components representing the host structure $E_{mi}^{(r,s)}$, $F_{nj}^{(r,s)}$ and the components representing the piezo patches $Ep_{mi}^{(r,s)}$,$Fp_{nj}^{(r,s)}$ are defined as:

$$E_{mi}^{(r.s)} = \int_0^1 \frac{\partial^r X_m(\varepsilon)}{\partial\varepsilon^r}\frac{\partial^s X_i(\varepsilon)}{\partial\varepsilon^s}d\varepsilon \tag{69}$$

$$F_{nj}^{(r.s)} = \int_0^1 \frac{\partial^r Y_n(\varepsilon)}{\partial\eta^r}\frac{\partial^s Y_j(\eta)}{\partial\eta^s}d\eta \tag{70}$$

$$Ep_{mi}^{(r.s)} = \int_0^1 Px(\varepsilon) \frac{\partial^r X_m(\varepsilon)}{\partial \varepsilon^r} \frac{\partial^s X_i(\varepsilon)}{\partial \varepsilon^s} d\varepsilon \quad (71)$$

$$Fp_{nj}^{(r.s)} = \int_0^1 Py(\eta) \frac{\partial^r Y_n(\varepsilon)}{\partial \eta^r} \frac{\partial^s Y_j(\eta)}{\partial \eta^s} d\eta \quad (72)$$

$where\ m.i = 1.2.3. \ldots . N \quad n.j = 1.2.3. \ldots . N \quad r.s = 0.1.2$

11. Results and Discussion

The accuracy of the analytical model's solutions was validated by comparing them with results obtained from COMSOL, a commercial FEA software. A proper bonding of the host structure and the piezoelectric patches is utilized. The connection between the piezo-patches and the external resistive load was modeled using a circuit element. Table 1 provides information about the material properties of both the composite plate and piezo patches.

Table 1. Material Properties of composite plate and piezo patches

Properties	Composite Plate	Piezoelectric Material
Width(mm)	500	150
Length(mm)	500	150
Thickness(mm)	2,5	0,2
Mass Density(kg/m^3)	1500	7750
Poisson's Ratio	0,25	0,35
Piezoelectic Constant $\bar{e}_{31}$ [C/m^2]	-	-16,041
Permittivity Constant $\bar{\varepsilon}^s_{33}$ [nF/m]	-	9,56
Young Modulus (E_{11}) [GPa]	150	-
Transverse Elastic Modulus (E_{22}) [GPa]	10	-
Shear Elastic Modulus G_{12} [GPa]	6	-
Piezoelectric strain coefficient (d_{31})	-	-171 pm V^{-1}
Dielectric permittivity at constant strain (ε^s_{33})	-	9,5657 nF m^{-1}
Dielectric permittivity at constant stress (ε^T_{33})	-	1,5052 nF m^{-1}
Absolute permittivity (ε_0)	-	8,854 pF m^{-1}
Compliances of the piezoelectric patch	-	S_{11}:16,4 pm^2 N^{-1} S_{12}:5,74 pm^2 N^{-1} S_{66} :44,3 pm^2 N^{-1}

Modal analysis was performed to determine the mode shapes and natural frequencies. By employing the mode superposition method and considering the first ten vibration modes, the voltage and displacement frequency response functions (FRFs) were calculated. Then the voltage frequency response function and displacement frequency response function of the system under 1 N load were found. In the following section, the power obtained from the system is discussed and the power outputs and average power outputs resulting from the optimizations are extracted.

12. Natural frequencies of system

The modal analysis of composite plates with surface-bonded piezo-patches is accomplished by employing both the Rayleigh-Ritz method and finite element simulations. The obtained solution for modal analysis is presented in Table 2, which displays the initial ten resonance frequencies of the system.

Table 2. First six natural frequencies of the different laminated plate

$V1 = 1, V3 = 1, [0/0]_s$			$V1 = 0, V3 = -1\ [45/-45]_s$			$V1 = -1, V3 = 1\ [90/90]_s$			$V1 = 0, V3 = 0\ [0/45/-45/90]_s$		
R-R	FEM	Diff.(%)	R-R	FEM	Diff.(%)	R-R	FEM	Diff.(%)	R-R	FEM	Diff.(%)
98,79	98,627	0,170	91,08	91,11	0,035	98,79	98,627	0,170	97,65	97,70	0,053
134,23	133,47	0,570	175,74	175,70	0,020	134,23	133,47	0,570	170,10	169,96	0,084
207,96	208,76	0,384	213,49	213,74	0,118	207,96	208,76	0,384	249,60	249,89	0,117
277,54	277,63	0,031	283,06	283,97	0,320	277,54	277,63	0,031	286,47	288,01	0,535
301,98	297,07	1,653	348,50	350,11	0,460	301,98	297,07	1,653	323,22	323,91	0,212
309,69	310,04	0,114	373,00	374,33	0,354	309,69	310,04	0,114	414,54	415,38	0,202
352,22	353,11	0,253	399,08	399,96	0,219	352,22	353,11	0,253	450,94	451,52	0,129
422,70	422,09	0,144	485,24	487,04	0,369	422,70	422,09	0,144	475,14	475,91	0,162
426,42	422,9	0,833	536,40	537,74	0,249	426,42	422,9	0,833	544,67	545,38	0,130
528,85	530,7	0,348	551,36	553,38	0,365	528,85	530,7	0,348	557,99	559,46	0,262

The abbreviation R-R represents the Rayleigh-Ritz method, while the subsequent columns represent the outcomes obtained from the analytical solution. The term FEA signifies the finite element method, and the subsequent columns illustrate the results obtained using COMSOL. It is important to note that in all the scenarios considered, the piezo patches are positioned at the plate's center. The analytical model and the COMSOL model match well and exhibit a discrepancy of no more than 1%.

13. Harmonic analysis for displacement FRFs and voltage FRFs

To calculate the frequency response function (FRF), a transverse point force of 1 N is applied at the upper section of the primary structure, specifically at position coordinates of (125) mm. The resulting vibrations are measured at coordinates of (375) mm. The subsequent graphs depict the displacement FRFs for the $[0/0]_s$, $[90/90]_s$, $[45/-45]_s$, and $[0/45/-45/90]_s$ lamination sequences. These FRFs are obtained for ten different modes utilized in both the analytical and finite element analysis solutions. To acquire the frequency response function (FRF) for voltage-to-force input, the voltage output across the resistive load needs to be measured. In both analytical and finite element modeling, a resistance value of 1e6 Ω is utilized, which closely resembles an open circuit condition. The voltage FRFs, or frequency response functions, for ten distinct modes are presented in the following graphs. These graphs depict the voltage FRFs for three different lamination sequences: $[0/0]_s$, $[90/90]_s$, $[45/-45]_s$, and $[0/45/-45/90]_s$. These FRFs are calculated using analytical solutions and FEM.

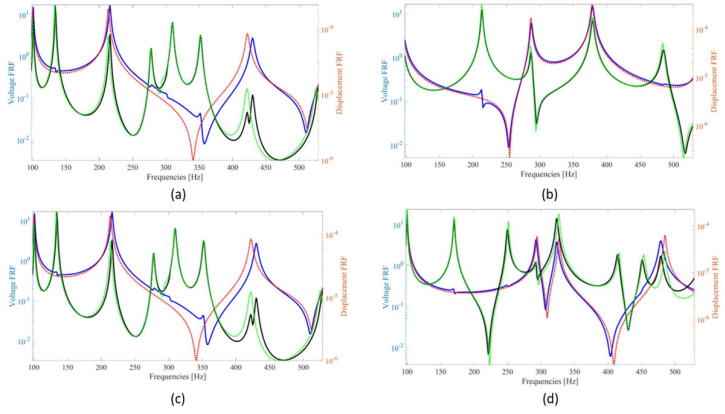

Fig. 8. Displacement and voltage FRF of system for different lamination sequences: $[0,0]_s$, (b) $[45, -45]_s$, (c) $[90,90]_s$, (d) $[90,90]_s$

14. Power outputs optimization

In this section, the maximum power outputs and the average values of the power outputs for a composite plate of 50x50cm dimensions with a 150×150mm piezoelectric patch integrated on its top surface are calculated. The power output can be derived from :

$$Power\ Output\ = \frac{V^2}{R_l} \tag{73}$$

Within this equation, V denotes the voltage output, and R_l represents the resistance of the load that can be derived as :

$$R_l = \frac{1}{Cpc * \omega_1,} \tag{74}$$

where C_{pc} is capacitance and the first natural frequency is ω_1. Optimization problems concerning lamination parameters find ideal solutions through the brut-force optimization by varying lamination parameters with increment of 0.01 values. This section shows the power outputs and the average of the power outputs obtained with different lamination parameters The size of the piezoelectric patch was taken as 150×150 mm for all cases.

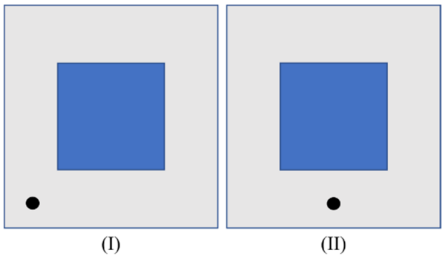

Fig. 9. Representation of the position of the forces (I) Force in the corner, (II) Force in the middle

First, a transverse load of 1 N was applied at 125 mm (coordinates on the *x*-axis and *y*-axis ($x_{i,1}$ and $y_{i,1}$) of the 500×500 mm composite plate with piezoelectric patch integrated and the power outputs were measured at 375 mm coordinates on the *x*- and *y*-axis ($x_{i,2}$ and $y_{i,2}$). Fig. 9(I). shows the position of the load. Then, a force of 1 N was applied on the composite plate of the same dimensions at the position coordinates, $x_{i,1}$=250 mm, $y_{i,1}$=125 mm, and measurements ($x_{i,2}$ and $y_{i,2}$) were taken over 375 mm. Also, Fig. 9. shows the position of the load. The table 10 shows the maximum power outputs and average power outputs for 2 different cases, as it can be seen the amount of maximum power output and also power average varies when the force location is changed and also it can be seen the improvement in maximum power output is higher compared to average power out in frequency range. Up to 48% improvement can be achieved by varying lamination parameters and this can significantly increase power out. As a result of the optimization depending on the lamination parameters, when the power output values are examined, the maximum power output is obtained at parameter values $V_1 = -0.4, V_3 = 0.7$ for the 50×50 cm composite plate and if the load is in the middle of bottom edge of the composite plate. For the composite plate of the same dimensions and if the load is at corner, the maximum power output is obtained at parameter values $V_1 = 0.2, V_3 = -0.9$.

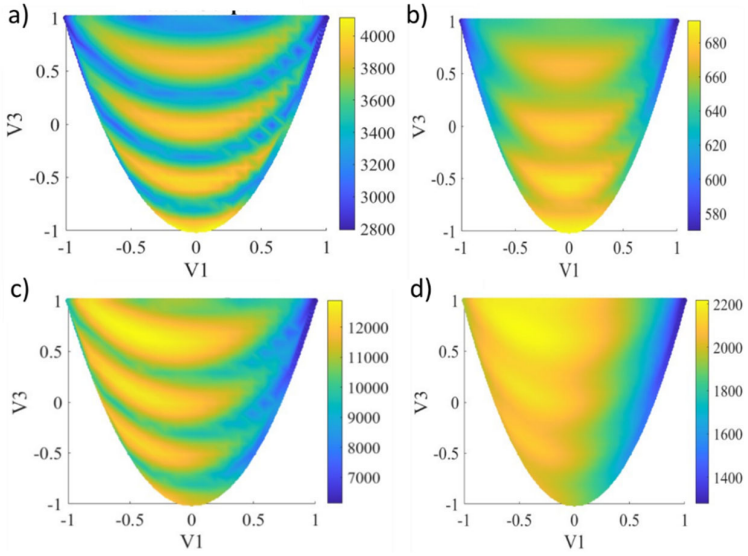

Fig. 10. a) maximum power out in case of force in the corner case (I), (b) average of power output in case of force in the corner case (I), c) maximum power out in case of force in the center case (II), (b) average of power output in case of force in the center case (II)

Loading location	$P_{out_{max}}$ Unidirectional [mW]	$P_{out_{max}}$ [mW]	Difference (%)	$P_{out_{average}}$ Unidirectional [mW]	$P_{out_{average}}$ [mW]	Difference (%)
Center	8675.25	12913.7	48.83	1645.2	2182.01	32.64
Corner	3060.85	4028.11	31.34	598.02	675.35	13.01

15. Conclusions

This paper investigates a new modeling approach to include the effect of lamination sequence by including lamination paraments in the design process. By utilizing the rayleigh-ritz method modal analysis was performed and validated via comparing to a commercial finite element software (FEM) COMSOL to provide accuracy, it was shown the method used in this paper has less than 1% difference with FEM. Furthermore, a thorough optimization was performed to show the optimum value of power output in smart composites. The research investigation conducted here reveals compelling evidence that the careful selection of proper lamination parameters have the potential to yield remarkable enhancements in the maximum power output of composite plates. To commence the study, the researchers delved into determining natural frequencies for distinct lamination parameters. Harmonic analyses were meticulously performed to gain valuable insights into the behavior of the composite plates under varying conditions. Subsequently, the researchers embarked on assessing the maximum power outputs and average values of the power outputs. This assessment encompassed a comprehensive exploration of diverse lamination parameters and composite materials, spanning a spectrum of sizes. Moreover, the findings offer an invaluable resource for advancing renewable energy systems, where the quest for greater energy generation and sustainability is paramount and by leveraging this newfound knowledge, engineers and designers can push the boundaries of what is achievable in these industries, driving progress and innovation toward a more sustainable and technologically advanced future.

References

Aghakhani, A., Lahe Motlagh, P., Bediz, B., & Basdogan, I. (2019). A general electromechanical model for plates with integrated piezo-patches using spectral-Tchebychev method. *Journal of Sound and Vibration*, *458*, 74–88.

Albazzan, M. A., Harik, R., Tatting, B. F., & Gürdal, Z. (2019). Efficient design optimization of nonconventional laminated composites using lamination parameters: A state of the art. *Composite Structures*, *209*, 362–374.

Bhat, R. B. (1985). Natural frequencies of rectangular plates using characteristic orthogonal polynomials in rayleigh-ritz method. *Journal of Sound and Vibration*, *102*(4), 493–499.

Cook-Chennault, K. A., Thambi, N., & Sastry, A. M. (2008). Powering MEMS portable devices—A review of non-regenerative and regenerative power supply systems with special emphasis on piezoelectric energy harvesting systems. *Smart Materials and Structures*, *17*(4), 043001.

Detwiler, D. T., Shen, M.-H. H., & Venkayya, V. B. (1995). Finite element analysis of laminated composite structures containing distributed piezoelectric actuators and sensors. *Finite Elements in Analysis and Design*, *20*(2), 87–100.

Erturk, A., & Inman, D. J. (2009). An experimentally validated bimorph cantilever model for piezoelectric energy harvesting from base excitations. *Smart Materials and Structures*, *18*(2), 025009.

Fakhzan, M. N., & Muthalif, A. G. A. (2013). Harvesting vibration energy using piezoelectric material: Modeling, simulation and experimental verifications. *Mechatronics*, *23*(1), 61–66.

Gohari, S., Sharifi, S., & Vrcelj, Z. (2016). New explicit solution for static shape control of smart laminated cantilever piezo-composite-hybrid plates/beams under thermo-electro-mechanical loads using piezoelectric actuators. *Composite Structures*, *145*, 89–112.

Howells, C. A. (2009). Piezoelectric energy harvesting. *Energy Conversion and Management*, *50*(7), 1847–1850.

Kim, H. S., Kim, J.-H., & Kim, J. (2011). A review of piezoelectric energy harvesting based on vibration. *International Journal of Precision Engineering and Manufacturing*, *12*(6), 1129–1141.

Lahe Motlagh, P., Bediz, B., Alan, S., & Kefal, A. (2023). Analysis of smart laminated composites integrated with piezoelectric patches using spectral element method and lamination parameters. *Journal of Sound and Vibration*, *567*, 118063.

Lam, K. Y., Peng, X. Q., Liu, G. R., & Reddy, J. N. (1997). A finite-element model for piezoelectric composite laminates. *Smart Materials and Structures*, *6*(5), 583–591.

Lee, C. K. (1990). Theory of laminated piezoelectric plates for the design of distributed sensors/actuators. Part I: Governing equations and reciprocal relationships. *The Journal of the Acoustical Society of America*, *87*(3), 1144–1158.

Li, H., Tian, C., & Deng, Z. D. (2014). Energy harvesting from low frequency applications using piezoelectric materials. *Applied Physics Reviews*, *1*(4), 041301.

Liu, X.-M. (2023). Mechanical response of composite materials prepared with polyurethane elastomers and polyvinyl chloride films. *Journal of the Mechanical Behavior of Biomedical Materials*, 106006.

Motlagh, P. L., Aghakhani, A., & Basdogan, I. (2018). Passive vibration control of a plate via piezoelectric shunt damping with FEM and ECM. *Smart Materials and Nondestructive Evaluation for Energy Systems IV*, *10601*, 8–15.

Motlagh, P. L., Anamagh, M. R., Bediz, B., & Basdogan, I. (2021). Electromechanical analysis of functionally graded panels with surface-integrated piezo-patches for optimal energy harvesting. *Composite Structures*, *263*, 113714.

Motlagh, P. L., Bediz, B., & Basdogan, I. (2020). A spectral Tchebychev solution for electromechanical analysis of thin curved panels with multiple integrated piezo-patches. *Journal of Sound and Vibration*, *486*, 115612.

Park, J. H., Hwang, J. H., Lee, C. S., & Hwang, W. (2001). Stacking sequence design of composite laminates for maximum strength using genetic algorithms. *Composite Structures*, *52*(2), 217–231.

Torres, E. O., & Rincon-Mora, G. A. (2009). Electrostatic Energy-Harvesting and Battery-Charging CMOS System Prototype. *IEEE Transactions on Circuits and Systems I: Regular Papers*, *56*(9), 1938–1948.

Tsai, S. W., & Hahn, T. (n.d.). *INTRODUCTION TO COMPOSITE MATERIALS*.

Wan, X., Cong, H., Jiang, G., Liang, X., Liu, L., & He, H. (2023). A Review on PVDF Nanofibers in Textiles for Flexible Piezoelectric Sensors. *ACS Applied Nano Materials*, *6*(3), 1522–1540.

Yang, B., Lee, C., Xiang, W., Xie, J., Han He, J., Kotlanka, R. K., Low, S. P., & Feng, H. (2009). Electromagnetic energy harvesting from vibrations of multiple frequencies. *Journal of Micromechanics and Microengineering*, *19*(3), 035001.

Yang, H., Guo, M., Wang, L., Hou, Y., Zhao, Q., Cao, D., Zhou, B., & Wang, D. (2017). Investigation on the factors influencing the performance of piezoelectric energy harvester. *Road Materials and Pavement Design*, *18*(sup3), 180–189.

Yoon, H., Youn, B. D., & Kim, H. S. (2016). Kirchhoff plate theory-based electromechanically coupled analytical model considering inertia and stiffness effects of a surface-bonded piezoelectric patch. *Smart Materials and Structures*, *25*(2), 025017.

Zhang, Y. X., & Yang, C. H. (2009). Recent developments in finite element analysis for laminated composite plates. *Composite Structures*, *88*(1), 147–157.

Zhou, M., Al-Furjan, M. S. H., & Wang, B. (2018). Modeling and Efficiency Analysis of a Piezoelectric Energy Harvester Based on the Flow Induced Vibration of a Piezoelectric Composite Pipe. *Sensors*, *18*(12), Article 12.